Wideband Reconfigurable Intelligent Surfaces with Frequency-Dependent Phase Quantization

Gerald C. Nwalozie, Liana Khamidullina*, Mehrab Ramzan‡, Padmanava Sen‡, and Martin Haardt**

*Communication Research Laboratory, Ilmenau University of Technology, Ilmenau, Germany

‡Barkhausen Institut, Dresden, Germany

email: gerald-chetachi.nwalozie@tu-ilmenau.de, liana.khamidullina@tu-ilmenau.de, mehrab.ramzan@barkhauseninstitut.org, padmanava.sen@barkhauseninstitut.org, martin.haardt@tu-ilmenau.de

***Abstract*—Reconfigurable Intelligent Surfaces (RIS) have emerged as a promising technology for beyond 5G and 6G networks due to their ability to enhance wireless communication performance through passive beamforming. While much of the existing literature focuses on narrowband systems, real-world applications demand efficient wideband RIS solutions. In this paper, we investigate an RIS-assisted wideband orthogonal frequency-division multiplexing (OFDM) communication system, incorporating discretized frequency-dependent reflection characteristics obtained and extended using electromagnetic (EM) simulations. Specifically, we implement a tunable passive artificial magnetic conductor (PAMC)-based RIS using a high-frequency structural simulator (HFSS) to extract realistic reflection phase angles near the desired frequency of 10 GHz. These profiles are quantized into two tunable frequency-dependent magnitudes and phase levels to accommodate hardware constraints and are applied to a downlink RIS-assisted wideband system. We propose a system model and optimization framework that accounts for frequency-dependent magnitudes and phase shifts of the reflection coefficients, and we show that although an RIS-assisted system with multiple subcarriers cannot achieve the spectral efficiency of a single-carrier system, it can still increase the total achievable rate in practical wideband communication scenarios.**

***Index Terms*—RIS, phase shift quantization, passive artificial magnetic conductor, multi-carrier.**

I. Introduction

Reconfigurable intelligent surfaces (RISs), also known as intelligent reflecting surfaces (IRSs), have received great attention from the research community as one of the promising technologies for beyond 5G (B5G) and 6G wireless networks. An RIS is a 2D planar surface with a large number of inexpensive tunable elements, e.g., antennas or metamaterials [1], [2]. The phase shifts of the RIS elements can be designed to meet a certain design objective, e.g., the reflected signals add constructively at the intended users and/or destructively at the unintended users [3]. Recently, various RIS-aided communication systems have been studied exploiting the reconfigurability potentials of RIS. These include cognitive radio systems, unmanned aerial vehicle (UAV), millimeter-wave (mmWave) communications, and dynamic time division duplex (DTDD) based communication systems [4]–[8].

Even though RIS potentials have been exploited in many applications, most of the existing works are focused on flat-fading narrowband systems [4]–[9]. In an RIS-assisted narrowband system, a single narrowband beamformer is designed for the single carrier [10]. However, the problem of beamformer design in a general wideband frequency-selective system is more difficult to solve since the RIS reflection pattern has to be designed for all subcarriers. This is because, for a wideband system, the phase shift and the amplitude of the reflected signals will vary with the frequencies of the incident signals [11]. Nevertheless, few works have studied the exploitation of the reconfigurable potentials of the RIS for wideband orthogonal frequency division multiplexing (OFDM) systems, e.g., [12]–[17]. In [17], the authors use a space-frequency Fourier transformation and the stationary phase method to derive an approximate closed-form solution for the RIS phase shifts. An RIS-aided wideband MIMO system using low-resolution analog-to-digital converters (ADC) was studied in [16]. A frequency reflection modulation (FRM) method is adopted for the modulation of the frequency of the incident electromagnetic wave for RIS-aided OFDM systems in [14]. In the reference, the RIS information is embedded in the frequency-hopping states of the RIS elements. The work in [15] models the RIS elements as a Lorentzian frequency response, which depicts the parameters that can be externally controlled to adjust the RIS's reflection profile. However, in such works, for ease of simplification, some unrealistic design assumptions are made which are practically difficult to implement due to hardware circuit limitations, especially for wideband structures [18]. As a result, for wideband systems, there is a need to implement realistic RIS reflection models.

In this paper, we consider an RIS-assisted OFDM communication system. We present preliminary results on enhancing wideband communication system performance through an extension of an experimentally validated reflecting surface with two quantization levels, capable of steering the reflected signal to 30° [19]. The realistic frequency-dependent behavior of the unit cells is extended to two tunable quantization levels by employing a transmission line loaded with an RF switch, enabling dynamic beam steering in different directions. Moreover, the impact of the surface's frequency-dependent behavior on communication system performance over a wide frequency band is investigated. Furthermore, we investigate how the frequency-dependent behavior of the surface over the 8-12 GHz range impacts communication system performance

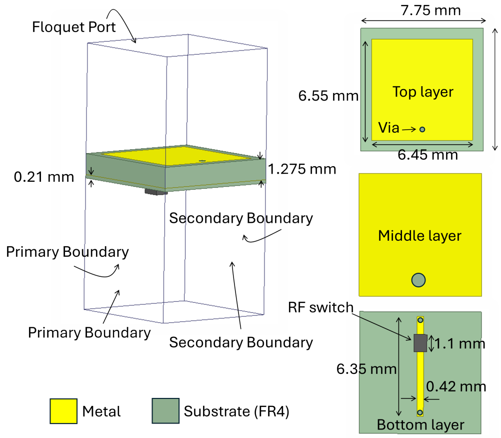

Fig. 1: EM simulation environment of the two-state RIS developed using three three-layer PCB design with an RF switch

in terms of spectral efficiency and achievable rates.

II. Design of RIS

In order to extract the frequency-dependent reflection phase and magnitude response of the planar reflecting intelligent surface, unit cell simulations are performed in an HFSS EM environment [20] using periodic boundary conditions with a Floquet port, as depicted in Fig. 1. The unit cell is based on a PAMC [19], which is made tunable with the help of a transmission line loaded with an RF switch. Fig. 1 shows the detailed configuration of the unit cell with its highlighted dimensions. The whole board is realized on three three-layer FR4 substrates, which have a permittivity of 4.6 and a loss tangent of 0.027. The top layer consists of a small metallic patch (highlighted in yellow), the middle layer consists of a full ground plane, and the bottom layer incorporates a 50 Ohm transmission line loaded with an RF switch. Inter-layer vias[1] are used to connect one end of the bottom transmission line with the top patch and the second end to the middle-layer ground plane. The switch ON and OFF configurations can be used to terminate the transmission line into a short and open circuit in order to have two different phase responses at 10 GHz, as shown in Fig. 2.

III. System Model

We consider a downlink communication system with a single antenna transmitter and a single antenna[2] receiver. The communication is aided by an RIS as shown in Fig. 3. The RIS has M_{S} reflecting elements, and we assume a 2D structure for the RIS such that $M_{\mathrm{S}} = M^{\mathrm{h}} \cdot M^{\mathrm{v}}$. We focus on a challenging scenario where the *direct link* is not available due to unfavorable propagation conditions. The channel model is

[1]Note: Via is a shortening pin used to connect different layers of PCB.

[2]Since the main focus of this paper is to analyze the performance of communication systems under realistic frequency-dependent and quantized RIS, for notational simplicity and page constraints, we consider a simple SISO scenario.

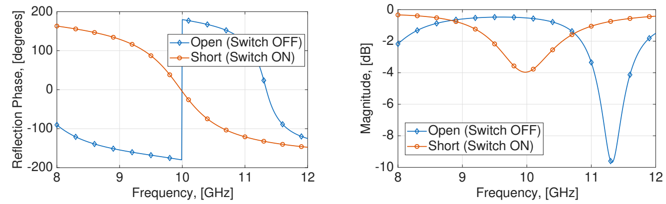

(a) Phase. (b) Magnitude.

Fig. 2: Frequency-dependent behavior of the 1-bit RIS based on an RF switch.

based on an OFDM with N subcarriers. The channel between the transmitter and the RIS is denoted as $\boldsymbol{h}_{\mathrm{T}} \in \mathbb{C}^{M_{\mathrm{S}}}$ and the channel vector between RIS and the receiver is defined as $\boldsymbol{h}_{\mathrm{R}} \in \mathbb{C}^{M_{\mathrm{S}}}$. The channel $\boldsymbol{h}_{\mathrm{R}}$ for the nth subcarrier is given as

$$\boldsymbol{h}_{\mathrm{R},n} = \sqrt{\frac{M_{\mathrm{S}}}{L_{\mathrm{R}}}} \sum_{\ell=1}^{L_{\mathrm{R}}} \xi_\ell e^{j2\pi f_n \tau_{\mathrm{R},\ell}} \boldsymbol{a}_{\mathrm{R}}(\mu_\ell^{\mathrm{h}}, \mu_\ell^{\mathrm{v}}), \tag{1}$$

where $\boldsymbol{a}_{\mathrm{R}}(\mu_\ell^{\mathrm{h}}, \mu_\ell^{\mathrm{v}})$ is the array steering vector at the RIS, μ_ℓ^{h} and μ_ℓ^{v} are the spatial frequencies of the ℓth path at the RIS. Scalars ξ_ℓ and $\tau_{\mathrm{R},\ell}$ represent the complex-valued channel gain and the delay of the ℓth path, respectively. Note that due to the 2D structure of the RIS, the array steering vector at the RIS is given as[3]

$$\boldsymbol{a}_{\mathrm{R}}(\mu_\ell^{\mathrm{h}}, \mu_\ell^{\mathrm{v}}) = \boldsymbol{a}_{\mathrm{R}}(\mu_\ell^{\mathrm{h}}) \diamond \boldsymbol{a}_{\mathrm{R}}(\mu_\ell^{\mathrm{v}}) \in \mathbb{C}^{M_{\mathrm{S}} \times 1}, \tag{2}$$

where the array steering vectors $\boldsymbol{a}_{\mathrm{R}}(\mu_\ell^{\mathrm{h}}) \in \mathbb{C}^{M^{\mathrm{h}} \times 1}$ and $\boldsymbol{a}_{\mathrm{R}}(\mu_\ell^{\mathrm{v}}) \in \mathbb{C}^{M^{\mathrm{v}} \times 1}$ have the following structures

$$\boldsymbol{a}_{\mathrm{R}}(\mu_\ell^{\mathrm{h}}) = \begin{bmatrix} 1 & e^{-j\mu_\ell^{\mathrm{h}}} & \cdots & e^{-j(M^{\mathrm{h}}-1)\mu_\ell^{\mathrm{h}}} \end{bmatrix}^{\mathsf{T}} \in \mathbb{C}^{M^{\mathrm{h}} \times 1}, \tag{3}$$

$$\boldsymbol{a}_{\mathrm{R}}(\mu_\ell^{\mathrm{v}}) = \begin{bmatrix} 1 & e^{-j\mu_\ell^{\mathrm{v}}} & \cdots & e^{-j(M^{\mathrm{v}}-1)\mu_\ell^{\mathrm{v}}} \end{bmatrix}^{\mathsf{T}} \in \mathbb{C}^{M^{\mathrm{v}} \times 1}. \tag{4}$$

The channel $\boldsymbol{h}_{\mathrm{T},n} \in \mathbb{C}^{M_{\mathrm{S}}}$ between the transmitter and the RIS is given as

$$\boldsymbol{h}_{\mathrm{T},n} = \sqrt{\frac{M_{\mathrm{S}}}{L_{\mathrm{T}}}} \sum_{\ell=1}^{L_{\mathrm{T}}} \kappa_\ell e^{j2\pi f_n \tau_{\mathrm{T},\ell}} \boldsymbol{a}_{\mathrm{T}}(\psi_\ell^{\mathrm{h}}, \psi_\ell^{\mathrm{v}}), \tag{5}$$

where κ_ℓ is the complex-valued channel gain of the ℓth path, $\boldsymbol{a}_{\mathrm{T}}(\psi_\ell^{\mathrm{h}}, \psi_\ell^{\mathrm{v}})$ is the array steering vector at the RIS, and n denotes the subcarrier index. We note that $\boldsymbol{a}_{\mathrm{T}}(\psi_\ell^{\mathrm{h}}, \psi_\ell^{\mathrm{v}})$ is defined similar to (1) above. Therefore, the received signal at the receiver for the nth subcarrier is expressed as

$$\begin{aligned} y_n &= \boldsymbol{h}_{\mathrm{R},n}^{\mathsf{T}} \boldsymbol{\Theta}_n \boldsymbol{h}_{\mathrm{T},n} \sqrt{P} x_n + z_n \qquad (6) \\ &= \boldsymbol{h}_n^{\mathsf{T}} \boldsymbol{\theta}_n \sqrt{P} x_n + z_n, \qquad (7) \end{aligned}$$

[3]**Notation:** Matrices and vectors are denoted by upper-case ($\boldsymbol{X}$) and lower-case ($\boldsymbol{x}$) bold-faced letters, respectively. The matrix transpose is denoted as $\boldsymbol{X}^{\mathsf{T}}$. Moreover, $\mathrm{diag}\{\boldsymbol{x}\}$ forms a diagonal matrix $\boldsymbol{X}$ by putting the entries of the input vector $\boldsymbol{x}$ in its main diagonal, while $\mathrm{bdiag}\{\boldsymbol{x}_1, \ldots, \boldsymbol{x}_N\}$ is the operation of constructing a block-diagonal matrix with the input vectors on the main diagonal. Furthermore, $\mathrm{mod}[\cdot]$ denotes the modulo 2π operation, $\|\boldsymbol{a}\|_2$ represents the 2-norm, $\odot$ and $\diamond$ denote the element-wise product and the Khatri-Rao product, respectively.

where $\boldsymbol{h}_n = \text{diag}\{\boldsymbol{h}_{\text{R},n}\}\boldsymbol{h}_{\text{T},n} \in \mathbb{C}^{M_\text{S}\times 1}$, P is the transmit power at the transmitter, z is the AWGN with σ^2 as the noise variance, and $\boldsymbol{\Theta}_n = \text{diag}\{\boldsymbol{\theta}_n\} \in \mathbb{C}^{M_\text{S}\times M_\text{S}}$ is the diagonal RIS phase shift matrix for the nth subcarrier with

$$\boldsymbol{\theta}_n = [\beta_{1,f_n} e^{j\phi_{1,f_n}}, \cdots, \beta_{M_\text{S} f_n} e^{j\phi_{M_\text{S} f_n}}]^\mathsf{T} \in \mathbb{C}^{M_\text{S}\times 1}, \quad (8)$$

where ϕ_{m,f_n} and β_{m,f_n} denote the reflection angle and the magnitude, respectively. We assume that the phase and the magnitude can be set to one of the $B = 2^b$ states, where b is the number of bits used for the quantization. Fig. 2 depicts the two states of the one-bit phase and magnitude quantization. Stacking the N received signals in a column vector, i.e., $\boldsymbol{y} = \{y_n\}_{n=1}^N \in \mathbb{C}^{N\times 1}$, we can express the received signal as

$$\begin{aligned}\boldsymbol{y} &= \sqrt{P}\begin{bmatrix}\boldsymbol{h}_1^\mathsf{T}\boldsymbol{\theta}_1 x_1\\ \vdots \\ \boldsymbol{h}_N^\mathsf{T}\boldsymbol{\theta}_N x_N\end{bmatrix} + \boldsymbol{z} &(9)\\ &= \sqrt{P}\text{bdiag}\{\boldsymbol{h}_1^\mathsf{T}, \cdots, \boldsymbol{h}_N^\mathsf{T}\}\text{bdiag}\{\boldsymbol{\theta}_1, \cdots, \boldsymbol{\theta}_N\}\boldsymbol{x} + \boldsymbol{z} &(10)\\ &= \sqrt{P}\text{diag}\{\boldsymbol{h}_1^\mathsf{T}\boldsymbol{\theta}_1, \cdots, \boldsymbol{h}_N^\mathsf{T}\boldsymbol{\theta}_N\}\boldsymbol{x} + \boldsymbol{z} &(11)\\ &= \sqrt{P}\boldsymbol{G}\boldsymbol{x} + \boldsymbol{z}. &(12)\end{aligned}$$

Therefore, the signal-to-noise ratio (SNR) is given as

$$\text{SNR} = \frac{P\|\boldsymbol{g}\|_2^2}{\sigma^2 N}, \quad (13)$$

where $\boldsymbol{g}$ is expressed as

$$\boldsymbol{g} = \text{diag}\{\boldsymbol{G}\} = \begin{bmatrix}\boldsymbol{h}_1^\mathsf{T}\boldsymbol{\theta}_1\\ \vdots \\ \boldsymbol{h}_N^\mathsf{T}\boldsymbol{\theta}_N\end{bmatrix} = \underline{\boldsymbol{h}}_1 \odot \underline{\boldsymbol{\theta}}_1 + \cdots + \underline{\boldsymbol{h}}_{M_\text{S}} \odot \underline{\boldsymbol{\theta}}_{M_\text{S}}, \quad (14)$$

with $\underline{\boldsymbol{h}}_m \in \mathbb{C}^N$ and $\underline{\boldsymbol{\theta}}_m \in \mathbb{C}^N$ denoting the channel and the phase vectors corresponding to the mth RIS element, respectively. The vectors $\underline{\boldsymbol{h}}_m \in \mathbb{C}^N$ and $\underline{\boldsymbol{\theta}}_m \in \mathbb{C}^N$ can be seen as columns of the matrices $\boldsymbol{H} = \left[\boldsymbol{h}_1^\mathsf{T}; \ldots; \boldsymbol{h}_N^\mathsf{T}\right] \in \mathbb{C}^{N\times M}$ and $\boldsymbol{\Theta} = \left[\boldsymbol{\theta}_1^\mathsf{T}; \ldots; \boldsymbol{\theta}_N^\mathsf{T}\right] \in \mathbb{C}^{N\times M}$, respectively. Then, in a 1-bit quantization case, the $\underline{\boldsymbol{\theta}}_m$ is restricted to one of the states depicted in Fig. 2. This means that in a wideband scenario, selecting an optimal reflection state for one frequency may lead to suboptimal phases for other frequencies, because the different frequencies cannot be optimized individually and are constrained to the same RIS state. The objective is to maximize the SNR at the receiver by optimizing the passive reflection coefficients of the RIS. We need to optimize the RIS reflection coefficients to have a constructive superposition at the receiver [3], [21] to achieve this objective. In the following, we evaluate the receiver's SNR by using measurement-based phase quantization for the RIS optimization for all the subcarriers.

IV. RIS Optimization

To begin, we note that to achieve a constructive superposition at the receiver, it implies that the RIS reflection coefficients should be designed such that all the phases of the components in (14) will add up constructively, i.e.,

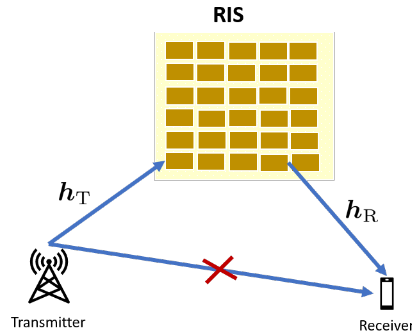

Fig. 3: An RIS-aided SISO communication system

$\angle\{\underline{\boldsymbol{h}}_1 \odot \underline{\boldsymbol{\theta}}_1\} = \cdots = \angle\{\underline{\boldsymbol{h}}_{M_\text{S}} \odot \underline{\boldsymbol{\theta}}_{M_\text{S}}\}$. As noted in the previous section, we consider a communication scenario with no direct path between the transmitter and receiver (see Fig. 3). Consequently, as long as the phases of all $\underline{\boldsymbol{h}}_m \odot \underline{\boldsymbol{\theta}}_m$, $m \in 1, \ldots, M_\text{S}$ overlap, the SNR depends only on the amplitudes of the channel vectors [22]. Therefore, assuming continuous phases and a *single subcarrier* system, to obtain the optimal RIS phase shifts that maximize the signal power in (14), we can choose a reference RIS element with an arbitrary phase shift and calculate the phases for the remaining RIS elements such that

$$\epsilon_r + \psi_r = \epsilon_i + \psi_i, \; i = 1, 2, \cdots, M_\text{S} - 1, \quad (15)$$

where ϵ_r and ψ_r are the channel and RIS phases for the selected reference element, and ϵ_i and ψ_i are the phases for the channel and RIS of the element we want to calculate. Therefore, the solution for the optimal phase-shift for the remaining RIS elements is given as [3]

$$\psi_i^{(\text{opt})} = \text{mod}\left[\epsilon_r - \epsilon_i + \psi_r\right]. \quad (16)$$

Considering a practical *multi-carrier* system, where the phase shifts of the RIS elements are subject to finite quantization and the reflection angles and magnitudes depend on the signal frequency as depicted in Fig. 2, the optimal solution in (16) cannot be achieved anymore. Therefore, we find a suboptimal solution for $\underline{\boldsymbol{\theta}}_i, i \in \{1, \cdots, M_\text{S}\}, i \neq r$ from the measurement bits in Fig. 2, such that the squared norm of the vector $\boldsymbol{g}$ given in (14), i.e.,

$$\|\boldsymbol{g}\|_2^2 = \|\underline{\boldsymbol{h}}_r \odot \underline{\boldsymbol{\theta}}_r + \underline{\boldsymbol{h}}_i \odot \underline{\boldsymbol{\theta}}_i\|_2^2, \quad (17)$$

is maximized. Here, the $\underline{\boldsymbol{\theta}}_r$ and $\underline{\boldsymbol{h}}_r$ denote the quantized RIS phases and the channel for the reference RIS element r, chosen as the element that corresponds to the channel with the highest power $\max_{i\in m}\{\|\underline{\boldsymbol{h}}_i\|_2^2\}$. This approach allows a direct selection of the RIS state from the quantized set of phases. Assuming a coarse quantization, i.e, with two or four candidate states, the solution of (17) can be computed with linear complexity $\mathcal{O}(M_\text{S} N)$

Another indirect approach is to compute the phase angles for the sensor i and all frequencies similar to (16) as

$$\boldsymbol{\psi}_i = \text{mod}\left[\boldsymbol{\epsilon}_r - \boldsymbol{\epsilon}_i + \boldsymbol{\psi}_r\right] \quad (18)$$

and chose the closest quantized phase angles from the measurements as

$$\min\{\|\boldsymbol{\psi}_b - \boldsymbol{\psi}_i\|_2\}, \tag{19}$$

where $\boldsymbol{\psi}_b$ is one of the phase lines from Fig. 2a. Compared to (17), however, the approach in (18) does not take the frequency-dependence of the reflection magnitudes into account.

V. Simulation Results

In this section, we show simulation results to evaluate the performance of our proposed methods as compared to baseline schemes. For performance evaluation, we use the spectral efficiencies (SE) given as $\mathrm{C} = \log_2(1 + \mathrm{SNR})$ as the first performance metric. We assume that the RIS has a uniform rectangular array (URA) structure with $M^{\mathrm{h}} = 21$ and $M^{\mathrm{v}} = 21$ elements, which are uniformly spaced. For simplicity, we assume that the number of channel paths for both the transmitting and receiving channels are equal, i.e., $L_{\mathrm{T}} = L_{\mathrm{R}} = L = 4$, the path gains follow $\{\xi_\ell, \kappa_\ell\} \sim \mathcal{CN}(0, 1)$, and the corresponding DoD and/or DoA are uniformly distributed in $[-\pi, \pi]$. The path delays τ_ℓ, $\ell \in 1, \cdots, L$ are assumed to be uniformly distributed in $[0, 1]$. In our experiment, we consider a frequency range of 8-12 GHz with subcarrier spacings of 300 MHz.

We consider quantized RIS phase shifts and compare the following algorithms:

- RIS phases optimized for one frequency ("Q1F"), where we choose the reference sensor r and the reference frequency n_r and compute the phase angle for the sensor i, n_r according to (16) as

$$\psi_{i,n_r}^{(\mathrm{opt})} = \mathrm{mod}\left[\epsilon_{r,n_r} - \epsilon_{i,n_r} + \psi_{r,n_r}\right]. \tag{20}$$

  Thereafter, we select the closest quantized phase angle from the measurements according to Fig. 2. That phase bit defines the phase shifts for the remaining frequencies due to the frequency dependency as explained in the paragraph below (14).
- Optimized signal power for all frequencies ("QP"), where the phases are selected to maximize (17).
- Optimized phase angles for all frequencies ("QA"), where the phases are calculated according to (18) and (19).
- Fixed quantized phases ("QR"), where the selected phase angles are computed as in (18) and (19) for all frequencies but with quantized phases chosen as: $[\pi/4, 5\pi/4]$.

The phases with the corresponding bit index are chosen according to Fig. 2 for the calculation of the spectral efficiencies (SEs) and achievable rates in our simulations. We note that for all algorithms, the reference phase is one of the 2-bit phases from the measurements, i.e., we try 2 RIS states as a reference phase and choose one that leads to the highest signal power. We also compare the SE of the considered multi-carrier system with the SE of a single carrier system (denoted as "Q1S" in the simulation results figures) and with random phase shifts (denoted as "RN").

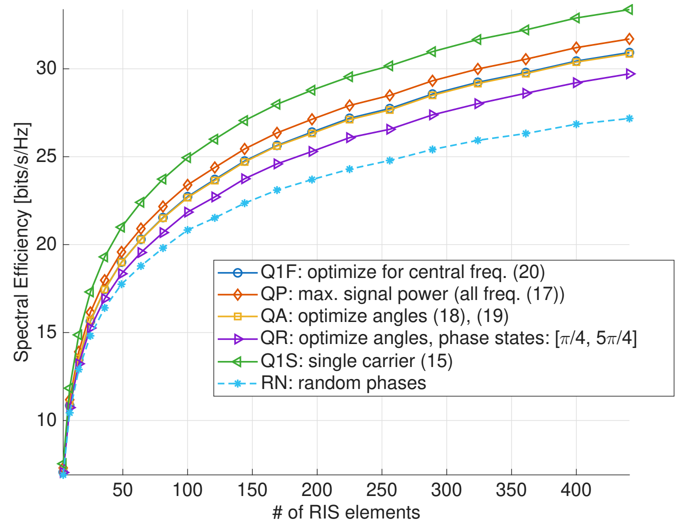

Fig. 4: Spectral Efficiency vs. Number of RIS elements. SNR = 5 dB. Results are averaged over 1000 channel realizations.

Fig. 4 depicts the spectral efficiencies for the RIS-aided SISO communication system as a function of the number of RIS elements. It can be seen that as the RIS size increases, the spectral efficiency of the system grows. We can also observe that the direct optimization of the squared norms in (17) provides the best performance results ("QP") among the curves corresponding to the wideband scenario since it allows selecting the best fit RIS state taking into account both phases and magnitudes. An approach where the continuous reflection angles are optimized according to (16) and (18) before applying the quantization, degrades the SE performance ("Q1F", "QA", "QR") as it does not account for channel and reflection magnitudes. The inferior performance of the "QR" curve demonstrates that optimizing the RIS subject to a fixed frequency-independent phase shifts considerably reduces the SE. Furthermore, the figure demonstrates that compared to the single carrier system ("Q1S"), the multiple subcarrier system shows only a 1-2 bits/s/Hz smaller SE and can still considerably increase the total achievable rate ($W \cdot \mathrm{SE}$, where $W = f^u - f^l$) in practical wideband communication scenarios as can be seen in Fig. 5, which depicts the rates as a function of the SNR.

VI. Conclusion

In this paper, we investigate the optimization of an RIS-assisted system with practical measurement-based quantized phase shifts. In contrast to the widely used narrowband assumption, we consider a realistic wideband communication scenario and present a system model and the corresponding optimization framework that accounts for quantized frequency-dependent magnitudes and phase shifts of the reflection coefficients. These realistic reflection coefficients are obtained via EM simulations, where a tunable PAMC-based RIS is implemented using HFSS. The two discrete magnitudes and phase shifts are frequency-dependent to accommodate hard-

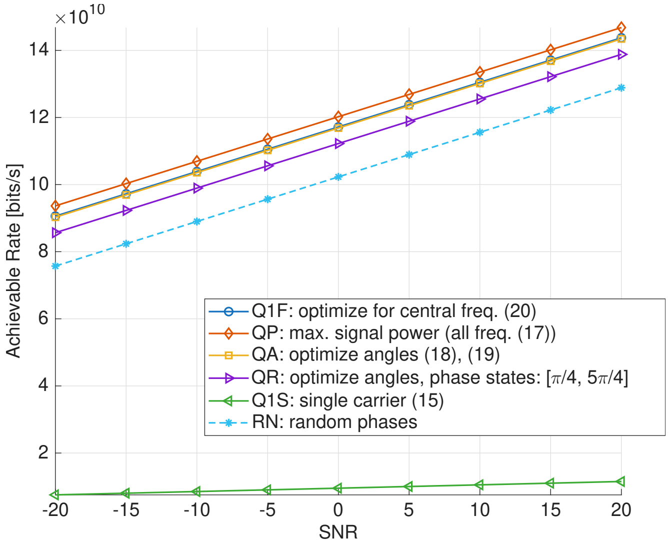

Fig. 5: Achievable rate vs. SNR. $L = 4$ paths, 1000 channel realizations, 21×21 RIS.

ware constraints and are used in a wideband SISO system. Our simulation results show that although an RIS-assisted system with multiple subcarriers cannot achieve the same spectral efficiency as a single-carrier system, it can still increase the total achievable rate in practical wideband communication scenarios significantly.

References

[1] M. Di Renzo, A. Zappone, M. Debbah, M. Alouini, C. Yuen, J. de Rosny, and S. Tretyakov, "Smart radio environments empowered by reconfigurable intelligent surfaces: How it works, state of research, and the road ahead," *IEEE Journal on Selected Areas in Communications*, vol. 38, no. 11, pp. 2450–2525, 2020.

[2] C. Liaskos, S. Nie, A. Tsioliaridou, A. Pitsillides, S. Ioannidis, and I. Akyildiz, "A new wireless communication paradigm through software-controlled metasurfaces," *IEEE Communications Magazine*, vol. 56, no. 9, pp. 162–169, 2018.

[3] Q. Wu, S. Zhang, B. Zheng, C. You, and R. Zhang, "Intelligent reflecting surface-aided wireless communications: A tutorial," *IEEE Transactions on Communications*, vol. 69, no. 5, pp. 3313–3351, 2021.

[4] Y. Cao, T. Lv, Z. Lin, and W. Ni, "Delay-constrained joint power control, user detection and passive beamforming in intelligent reflecting surface-assisted uplink mmwave system," *IEEE Transactions on Cognitive Communications and Networking*, vol. 7, no. 2, pp. 482–495, 2021.

[5] G. C. Nwalozie, K. Ardah, and M. Haardt, "Reflection Design methods for Reconfigurable Intelligent Surfaces-aided Dynamic TDD Systems," in *Proc. of IEEE 12th Sensor Array and Multichannel Signal Processing Workshop (SAM 2022)*, Jun. 2022.

[6] G. C. Nwalozie and M. Haardt, "Distributed Coordinated Beamforming for RIS-aided Dynamic TDD Systems," in *Proc. of 26th International ITG Workshop on Smart Antennas and 13th Conference on Systems, Communications, and Coding (WSA and SCC 2023), Braunschweig, Germany*, Feb. 2023.

[7] J. Yuan, Y. Liang, J. Joung, G. Feng, and E. G. Larsson, "Intelligent reflecting surface-assisted cognitive radio system," *IEEE Transactions on Communications*, vol. 69, no. 1, pp. 675–687, 2021.

[8] A. C. Pogaku, D. Do, B. M. Lee, and N. D. Nguyen, "UAV-assisted RIS for future wireless communications: A survey on optimization and performance analysis," *IEEE Access*, vol. 10, pp. 16 320–16 336, 2022.

[9] G. C. Nwalozie and M. Haardt, "Leakage-based Coordinated Beamforming for RIS-aided Dynamic TDD Systems," in *Proc. of 31st European Signal Processing Conference (EUSIPCO 2023), Helsinki, Finland*, September 2023.

[10] Z. Zhang, L. Dai, X. Chen, C. Liu, F. Yang, R. Schober, and H. V. Poor, "Active RIS vs. passive RIS: Which will prevail in 6G?" *IEEE Transactions on Communications*, vol. 71, no. 3, pp. 1707–1725, 2023.

[11] H. Li, W. Cai, Y. Liu, M. Li, Q. Liu, and Q. Wu, "Intelligent reflecting surface enhanced wideband MIMO-OFDM communications: From practical model to reflection optimization," *IEEE Transactions on Communications*, vol. 69, no. 7, pp. 4807–4820, 2021.

[12] Y. Yang, B. Zheng, S. Zhang, and R. Zhang, "Intelligent Reflecting Surface Meets OFDM: Protocol Design and Rate Maximization," *IEEE Transactions on Communications*, vol. 68, no. 7, pp. 4522–4535, 2020.

[13] B. Zheng and R. Zhang, "Intelligent reflecting surface-enhanced OFDM: Channel estimation and reflection optimization," *IEEE Wireless Communications Letters*, vol. 9, no. 4, pp. 518–522, 2020.

[14] W. Yan, X. Yuan, and X. Cao, "Frequency reflection modulation for reconfigurable intelligent surface aided ofdm systems," *IEEE Transactions on Wireless Communications*, vol. 21, no. 11, pp. 9381–9393, 2022.

[15] K. D. Katsanos, N. Shlezinger, M. F. Imani, and G. C. Alexandropoulos, "Wideband multi-user mimo communications with frequency selective riss: Element response modeling and sum-rate maximization," in *2022 IEEE International Conference on Communications Workshops (ICC Workshops)*, 2022, pp. 151–156.

[16] X. Chen, H. Ren, C. Pan, Z. Peng, K. Zhi, Y. Liu, X. Xi, A. G. Armada, and C.-X. Wang, "Performance analysis on ris-aided wideband massive mimo ofdm systems with low-resolution adcs," *IEEE Transactions on Wireless Communications*, pp. 1–1, 2025.

[17] X. Qian, X. Hu, C. Liu, and M. Peng, "Wideband beamforming with ris: A unified framework via space-frequency transformation," *IEEE Transactions on Signal Processing*, vol. 73, pp. 173–187, 2025.

[18] W. Tang, J. Y. Dai, M. Z. Chen, K.-K. Wong, X. Li, X. Zhao, S. Jin, Q. Cheng, and T. J. Cui, "MIMO transmission through reconfigurable intelligent surface: System design, analysis, and implementation," *IEEE Journal on Selected Areas in Communications*, vol. 38, no. 11, pp. 2683–2699, 2020.

[19] S. Al Nahiyan, M. Ramzan, S. Kamal, and P. Sen, "Passive Artificial Magnetic Conductor (AMC) Reflector for Far-Field Beam Steering," in *Proc. 54th European Microwave Conference (EuMC)*, 2024, pp. 533–536.

[20] ANSYS Inc., "ANSYS HFSS: High Frequency Structure Simulator, Version 2024 R1," Computer software, 2024, [Online]. Available: https://www.ansys.com/products/electronics/ansys-hfss.

[21] E. Björnson, Ö. T. Demir, and L. Sanguinetti, "A primer on near-field beamforming for arrays and reconfigurable intelligent surfaces," 2021. [Online]. Available: https://arxiv.org/abs/2110.06661

[22] E. Björnson, O. Özdogan, and E. G. Larsson, "Intelligent reflecting surface versus decode-and-forward: How large surfaces are needed to beat relaying?" *IEEE Wireless Communications Letters*, vol. 9, no. 2, pp. 244–248, 2020.